


RESEARCH ARTICLE

Open Access



Surface science on Phobos with the navigation cameras of the MMX IDEFIX rover

Pierre Vernazza^{1*} , Laurent Jorda¹, Simon Tardivel², Julien Baroukh², Olivier Groussin¹, Celia Pimorin¹, Axel Poulain¹, Pierre-Yves Chabaud¹, Emilie Robert², Jean Bertrand², Valerian Lалуcaa², Emile Remetean², Nicolas Théret², Cedric Virmontois², Naomi Murdoch³, Stéphane Le Mouélic⁴, Pierre Beck⁵, Ottaviano Rüsçh⁶, Jessica Flahaut⁷, Sebastien Charnoz⁸, Jeremie Lasue⁹, Maria-Antonietta Barucci¹⁰, Alain Doressoundiram¹⁰, Patrick Michel¹¹ and Stephan Ulamec¹²

Abstract

A CNES/DLR rover called IDEFIX will be deployed on the surface of Phobos in late 2028 or early 2029 as part of JAXA's Martian Moons eXploration (MMX) mission. The goal of the rover is to travel across the surface of Phobos for at least 100 days, with autonomous guidance provided by the navigation cameras (a stereo pair). By taking stereoscopic images of the area around IDEFIX up to the horizon (resolution of a few millimeters at 1 m), the navigation cameras aim to provide answers to a number of scientific questions, such as the origin of the color dichotomy, the nature of space weathering processes, and the extent of dust transport and exogenous contamination on Phobos. Here we present the IDEFIX navigation cameras, including their ground calibrations, and the science questions they are intended to address. We also present the architecture of the data processing pipeline being developed at the Laboratoire d'Astrophysique de Marseille to address the science objectives of the navigation cameras.

Keywords Phobos, In situ imaging, Regolith, Space weathering, Boulder cracking, Dust transport, Topography, Geomorphology

*Correspondence:

Pierre Vernazza
pierre.vernazza@lam.fr

¹ Aix Marseille Université, CNRS, CNES, LAM, Institut Origines, 38 rue Frederic Joliot Curie, 13013 Marseille, France

² CNES, 18 avenue Edouard Belin, 31401 Toulouse, France

³ ISAE-SUPAERO, Université de Toulouse, 10 avenue Edouard Belin, 31055 Toulouse, France

⁴ Laboratoire de Planétologie et Géosciences, CNRS, Nantes Université, Univ Angers, Le Mans Université, 44000 Nantes, France

⁵ Univ. Grenoble Alpes, CNRS, IPAG, Grenoble, France

⁶ Institut für Planetologie, Universität Münster, Münster, Germany

⁷ Université de Lorraine, CNRS, CRPG, Nancy, France

⁸ Université de Paris Cité, Institut de Physique du Globe de Paris, CNRS, 75005 Paris, France

⁹ Institut de Recherche en Astrophysique et Planétologie, Université de Toulouse 3 Paul Sabatier, CNRS, CNES, Toulouse, France

¹⁰ Observatoire de Paris, CNRS, LIRA, Université Paris Cité, Université PSL, Sorbonne Université, 92195 Meudon, France

¹¹ Laboratoire Lagrange, CNRS, Observatoire de la Côte d'Azur, Université Côte d'Azur, 06304 Nice, France

¹² German Aerospace Center, DLR, 51147 Cologne, Germany



© The Author(s) 2025. **Open Access** This article is licensed under a Creative Commons Attribution 4.0 International License, which permits use, sharing, adaptation, distribution and reproduction in any medium or format, as long as you give appropriate credit to the original author(s) and the source, provide a link to the Creative Commons licence, and indicate if changes were made. The images or other third party material in this article are included in the article's Creative Commons licence, unless indicated otherwise in a credit line to the material. If material is not included in the article's Creative Commons licence and your intended use is not permitted by statutory regulation or exceeds the permitted use, you will need to obtain permission directly from the copyright holder. To view a copy of this licence, visit <http://creativecommons.org/licenses/by/4.0/>.

1 Introduction

The origin of the Martian moons Phobos and Deimos remains an unresolved mystery, with two main competing hypotheses: (i) intact capture of two distinct solar system small bodies and (ii) accretion within an impact-generated disk. Solving this longstanding puzzle is key to understanding the evolutionary history of the formation region of the terrestrial planets (e.g., Ronnet et al. 2016; Rosenblatt et al. 2016; Hyodo et al. 2017; Canup and Salmon 2018; Barucci et al. 2021; Hyodo et al. 2022).

Phobos, the largest and closest moon to Mars, is the principal target of the Martian Moon eXploration (MMX) JAXA mission, which is scheduled for launch in 2026. The mission will orbit Phobos and perform multiple fly-bys of Deimos, send a rover to the surface of Phobos (Michel et al. 2022) and retrieve and return ≥ 10 g of Phobos regolith back to Earth in 2031 (Kuramoto et al. 2022; Kawakatsu et al. 2023). The primary objective of the mission is to provide a definitive answer regarding the origin of the Martian moons. Despite three previous attempts (Phobos 1 and 2 in 1988 and Phobos-Grunt in 2011, all of which were unsuccessful), there has been no dedicated mission to the Martian moons to date (Duxbury et al. 2014). The mission comprises an orbiter and a small rover, designated IDEFIX. The latter is a contribution from the Centre National d'Etudes Spatiales (CNES) and the German Aerospace Center (DLR).

The instrument suite on board the rover will comprise the navigation cameras (a stereo pair), two wheel cameras (Murdoch et al., this issue), a Raman spectrometer and a mini radiometer. The cameras (NavCams & Wheelcams) are a contribution from CNES, whereas the remaining two instruments are provided by DLR. In addition to performing in situ science, IDEFIX will act as a scout in order to prepare the main spacecraft for landing (Ulamiec et al. 2023). The current baseline predicts that IDEFIX will be released from the mother spacecraft in late 2028 or early 2029 at a height of less than 100 ms (ideally 40–50 ms). It will then descend ballistically to the surface of Phobos and come to rest in an arbitrary location after a few bounces. Following its landing, the rover will upright itself, deploy its solar panels, characterize the terrain in front of it, and commence its journey at a typical velocity of up to a few millimeters per second. The rover mission is foreseen to last at least 100 days. The surface terrain of Phobos will have a significant impact on the distance the rover can travel. A distance ranging from a few meters to 100 ms may be covered.

The present paper provides a summary of the design of the rover navigation cameras and of their science goals and describes the ground calibrations that have been performed. It also provides a description of the observation strategy. Finally, we present the architecture of the data

processing pipeline that is being developed to address the science objectives of the navigation cameras.

2 Scientific objectives

By performing stereoscopic imaging of the site surrounding IDEFIX, up to the horizon, the navigation cameras aim to provide answers—in a coordinated effort with orbiter and other rover instruments (*such as the TENGOO and OROCHI cameras* (Kameda et al. 2021) *and the MIRS spectrometer* (Barucci et al. 2021) *on the orbiter, the Wheelcams, miniRAD and RAX*)—to the following main scientific questions of the MMX mission concerning Phobos' surface geology:

- What is the link between geological/topographic features and spectrophotometric properties of Phobos' regolith?
- How does space weathering work on Phobos? Is it Lunar-like or Tagish Lake-like space weathering?
- What is the origin of the color dichotomy on Phobos?
- What is the occurrence of grooves and craters at small scales?
- What is the boulder/grain size distribution for $D \geq 3$ -mm particles and how does it compare with other small bodies?
- Are exogenous materials present? If yes, what is their composition and origin?
- How does erosion work for boulders and centimeter-sized rocks on Phobos? How common is boulder cracking and is it thermally or impact driven?
- Is there any evidence of dust transport and levitation on Phobos?

These science questions are grouped according to the following topics and presented in more detail in the following subsections:

- Topography and Morphology
- Scattering properties of the regolith
- Space weathering
- Exogenous contamination
- Compositional heterogeneity
- Boulder erosion
- Dust transport

2.1 Topography and Morphology

The navigation cameras' main purpose will be to determine with precision the topography of the landscape in front of the rover, such information being key for the locomotion. The collected images will allow digital terrain models (DTMs) to be delivered with a ground

sampling of about 1 mm for the first meter and an accuracy of a few millimeters at 1 m. Note that the first DTMs to be produced will be critical for constraining precisely the location and orientation of the rover by direct comparison with the high-resolution DTMs of the orbiter produced with the TENG00 data.

The high-resolution DTMs produced with the NavCams images along with the images themselves will be used to:

- produce a photo-geological map of each imaged scene (e.g., Jaumann et al. 2019)
- constrain the surface roughness/waviness
- characterize the size, shape and distribution of particles/boulders with diameters greater than a few millimeters and that of small impact craters
- identify groove-like patterns
- attempt to constrain the load-bearing strength of the regolith
- determine morphology and texture (clasts, joints) of boulders and/or outcrops (e.g., Otto et al. 2021)

The NavCam observations in tandem with the TENG00 and OROCHI ones will allow determining the crater cumulative number density (per km²) as a function of crater diameter down to a few tens of centimeters, thus allowing a characterization of the size frequency distribution (SFD) of the impactor population down to very small diameters (a few centimeters). Furthermore, the NavCam observations will allow bridging the gap between the SFDs of boulders and grains determined by the orbiter cameras and the rover wheelcams, leading to a continuous SFD of grains/boulders down to a few hundred microns when merging all MMX imaging observations. Such measurements will be key to estimate erosion processes such as boulder cracking.

Finally, the produced DTMs and collected images should allow estimating the penetration depth of the rover wheels, provided that the rover is able to travel a few meters at least, thus allowing an independent estimate from the one directly measured by the wheelcams. Such measurement will provide a constraint of the mechanical properties of the regolith, namely of its load-bearing strength (Bigot et al. 2024, Murdoch et al. this issue).

2.2 Scattering properties of the regolith

A wide-angle color camera landed on the surface of an atmosphereless body will provide a first characterization of Phobos' regolith light scattering properties, especially its phase function. Unlike spectroscopic measurements, which indicate the presence of different minerals, the phase function, and especially its associated opposition

effect, gives information on the regolith's physical properties such as particle sizes, optical indices, and porosity (see, e.g., Hapke 2012). In addition, the Bayer filter that the camera is equipped with will provide a first indication of the phase function variation with wavelength at the sub-cm scale, which can be linked to space weathering or roughness (e.g., Gradie and Veverka 1986).

Such characterizations have been done with cameras landed on other solar system bodies, like the Moon with the Yutu rovers (Jin et al. 2015; Lin et al. 2020) and Chang'E landers (Xu et al. 2022), Mars with the MER rovers (Johnson et al. 2006a, b, 2015, 2021) and Mars Science Laboratory (Johnson et al. 2022), asteroids like Itokawa (Lederer et al. 2005; Tatsumi et al. 2018), Ryugu (Tatsumi et al. 2020; Otto et al. 2023) and Bennu (Golish et al. 2021) and comet 67P/Churyumov-Gerasimenko (La Forgia et al. 2015; Otto et al. 2021).

Such in situ curves give a different set of informations complementary to the orbital one, given the small scale (typically centimetric) at which they are taken. The fitting of the phase function with the Hapke model can constrain from 3 to 9 regolith parameters depending on the number of observations and the complexity of the signal. Those parameters will typically include the single-scattering albedo value, a porosity parameter and asymmetric factors associated with Henyey-Greenstein functions fitting that characterize the forward and backward scattering properties of the material. Those values can then be compared to laboratory analogs and other solar system bodies to provide the larger context of Phobos' regolith properties.

2.3 Space weathering

Space weathering processes (irradiation by cosmic and solar wind ions and bombardment by interplanetary dust particles) alter the optical properties of planetary surfaces that are not protected by an atmosphere or a magnetosphere (see Brunetto et al. (2015) and Pieters and Noble (2016) for reviews). These processes must therefore be relevant at the surface of the Martian moons.

In the case of silicate-rich carbon-poor surfaces, these processes tend to darken and redden the optical properties of the surface. This is the case for Earth' moon and for so-called S-type asteroids. In the latter case, it was observed that asteroid surfaces age and redden in less than a million years. This timescale is compatible with the one obtained via laboratory ion irradiation experiments mimicking solar wind implantation but not with the one from experiments simulating micrometeorite bombardment, implying that the solar wind is the main agent responsible for the color change of S-type asteroid surfaces (Vernazza et al. 2009).

In the case of chondrule-poor carbonaceous chondrites such as CIs, CMs or Tagish Lake, the color trend is opposite to the one observed for silicate-rich surfaces, with an increase of the albedo and a bluish of the spectral slope in the optical domain (e.g., Lantz et al. 2018; Vernazza et al. 2013).

The two diverging trends described above are highly relevant for the interpretation of space weathering effects on Phobos. Phobos' visible and near-infrared spectrum is similar to both the Moon (silicate-rich) spectrum and the one of the Tagish Lake meteorite (Ronnet et al. 2016) with Phobos' albedo (~ 0.07) being in between that of P/D-type asteroids (~ 0.04 – 0.07 ; Mahlke et al. 2022 and references therein) and that of the Moon (~ 0.1 – 0.2 ; Xu et al. 2023 and references therein).

The spectrophotometric observations of fresh areas on Phobos (mass wasting, small craters, fractured rocks and if possible the rover tracks) with the NavCams will reveal how space weathering works on Phobos, including whether it reddens and darkens the surface (similar to Lunar-like), causes blueing (similar to Tagish Lake-like), or something different. Specifically, the images will allow to produce albedo and spectral slope maps in the 450–700 nm range using the color information from the RGGB filters (the spectral slope will be computed for each pixel as a linear fit across the R, G, G and B reflectance values). We expect the uncertainties of both quantities (albedo, slope) to be less than 10%.

2.4 Exogenous contamination

Contamination of Phobos' surface with foreign materials is a likely phenomenon as this seems to be a common alteration process of asteroid surfaces (e.g., McCord et al. 2012; Pieters et al. 2012; Vernazza et al. 2017; Tatsumi et al. 2021, 2022; DellaGiustina et al. 2021). At Vesta, carbonaceous chondritic material (McCord et al. 2012; Pieters et al. 2012; Reddy et al. 2012) was identified as the main contaminant, whereas on Ryugu and Bennu, mostly silicate-rich HED-like and ordinary chondrite-like materials were identified as contaminants (Tatsumi et al. 2021, 2022; DellaGiustina et al. 2021). In the case of Phobos, calculations by Ramsley and Head (2013) and Hyodo et al. (2019) suggest that minor amounts of Martian soil (~ 250 – 1000 ppm) may be mixed with its regolith, which does not exclude contamination by other sources.

The NavCam images will be used to produce albedo and low-resolution spectral maps in the 450–700 nm range allowing the detection of materials with very different albedo and spectral properties. It is worth mentioning that the critical 0.8–1 micron region in which silicates such as olivine and pyroxene possess a well-defined absorption feature will not be covered by the NavCams, precluding the identification of such materials.

Complementary observations with the rover wheelcams and the accompanying colored LEDs (Murdoch et al., this issue) will be precious in this respect.

More generally, the rover data are well suited to provide constraints on the amount of contamination of Phobos' surface and by extension that of small bodies in general with unprecedented precision. The previous detections in the asteroid cases listed above lacked the necessary angular resolution for tackling such questions.

2.5 Compositional heterogeneity

The surface of Phobos is heterogeneous, exhibiting two spatially coherent units. The red unit has a spectrum that slopes more steeply into the near-infrared, while the blue unit has a less red spectrum (e.g., Murchie et al. 1991; Murchie and Erard 1996). The red unit also exhibits a 0.65-micron absorption feature, whereas the blue unit is featureless in the visible domain. The blue unit is concentrated around the Stickney crater, suggesting a genetic relation between the two. As of today, however, no simple spatial distribution nor stratigraphic relation between the red and blue materials can be discerned.

The current plan is for IDEFIX to land on the anti-Mars side in late 2028 or early 2029. It follows that the NavCam observations will probably not contribute directly to our understanding of the large color dichotomy on the Mars-facing side. However, dust migration across the surface of Phobos after impacts cannot be ruled out, with blue materials possibly being present on the anti-Mars side. Observations made by the NavCams in conjunction with those made by the TENG00, OROCHI and MIRS instruments (Kameda et al. 2021; Barucci et al. 2021) will have a good chance of distinguishing blue from red materials and contribute to our understanding of how these materials have been altered, mixed and transformed into the regolith seen today, and whether blue and red materials also coexist on the anti-Mars side. In particular, the albedo and low-resolution spectral maps produced with the images will allow the identification of blue materials, should they be present. Along these lines, data in the red filter (around 700 nm) will be used to search for an absorption feature (indicative of red materials), thereby strengthening the distinction between blue and red materials.

2.6 Boulder erosion

The NavCam close-up observations of centimeter-scale rocks and larger boulders will provide unique information on rock morphology and texture (Section 2.1) as well as on rock erosion processes. In particular, on the atmosphere-less surface of Phobos, rocks should be affected by fracturing and fragmentation from meteoroid bombardment and by thermal stresses due to diurnal temperature

variations. The NavCam observations should, in principle, allow us to determine the importance of fracturing by thermal fatigue of centimeter and tens of centimeter wide rocks (e.g., Delbo et al. 2014, Molaro et al. 2020) and distinguish it from erosion by meteoroid bombardment. In the case of impact-generated cracks, we would expect them to be randomly oriented. In the case of thermal fatigue, where diurnal and annual thermal cycles induce crack growth in rocks, one would expect to observe cracks with a preferred orientation, namely perpendicular to the diurnal path of the heat source (Sun) on the surface (north–south direction; see Molaro et al. 2020 and references therein). This phenomenon has been observed on Earth and Mars (e.g., McFadden et al. 2005; Eppes et al. 2015). In the case of small asteroids such as Bennu and Ryugu, however, several processes will affect the alignment of thermal cracks, including material movement, reshaping and impacts. Despite these potential biases, the observed orientation of cracks on both objects suggests that thermal cycling is the primary driver of boulder degradation (e.g., Molaro et al. 2020; Sasaki et al. 2021).

We anticipate a similar situation at Phobos. To distinguish between thermal cracking and impact-generated cracks, we will identify cracks and measure their orientation with respect to the north–south direction and perform a statistical analysis of this distribution. Note that in the case of Phobos, due to the varying gravity field (Phobos' orbit is eccentric), boulders may be subject to surface movement. This effect, if present, may randomize the distribution of crack orientations to some extent.

In principle, the NavCams will be able to image a crack from multiple aspect angles as the rover approaches a boulder. Complementing orbital imagery, these multiple views will allow not only the direction of a crack to be estimated, but also the orientation of the three-dimensional fracture plane and thus better assess its origin (e.g., Schirner et al. 2024). Micrometeoroid bombardment should be recorded on boulder surfaces by spallation zones, pits and melt splashes (e.g., Hörz et al. 2020). Fractured and clustered boulders should also be expected due to fragmentation by meteoroid bombardment (e.g., Basilevsky et al. 2015; Ruesch et al. 2020; Ruesch and Bickel 2023).

2.7 Dust transport

Two main mechanisms can lead to dust transport across the surface of an airless body: impacts and electrostatic transport of dust particles charged by UV radiation and plasma irradiation (e.g., Rennilson and Criswell 1974; Criswell 1973; Colwell et al. 2005; Wang et al. 2016).

Dust levitation will be searched for via dedicated observations of the dusk horizon. It should be noted, however,

that the detection of a distinct glow, as observed on the Moon (Criswell 1973; Rennilson and Criswell 1974), may never occur if present, as it would imply substantial dust levitation leading to a rapid coverage of IDEFIX's solar panels (hence to a rapid loss of power).

In addition, the presence of dust on and around rocks and boulders (e.g., in the form of debris aprons) will be investigated. This spatial relationship with rock topography could lead to insights into impact-delivered dust, electrostatic transport of dust (e.g., Piquette and Horányi 2017) as well as new dust production. For example, dust could be produced from rocks by microflaking driven by diurnal thermal stresses (Patzek and Ruesch 2022) and/or micrometeoroid bombardment (Ruesch and Wöhler 2022). If data with sufficient variation in viewing and illumination geometry can be obtained, the study of the photometric properties of dust deposits at different distances from the boulders could be particularly informative in revealing dust properties and dynamics (e.g., Ruesch et al. 2024).

3 Instrument description

The NavCams are mounted at the top of the front panel of the rover and are tilted down by 23° (Fig. 1). The mass of the NavCams (stereo bench) is ~526 g. Four white LEDs are located in between the stereo camera to allow observations during the night. The NavCams consist of a stereoscopic pair with a field of view (diagonal) of 122°, a focal length (F) of ~7.9 mm, a $F/8$ aperture and a depth of field from 35 cm to infinity (Fig. 1). The stereo baseline (distance between the two cameras) is 6 cm. Each camera consists of a wide-angle optical lens assembly developed by Lambda-X (Fig. 2) and a CASPEX 2048×2048 pixels CMOS detector equipped with RGGB Bayer filters (Fig. 3) provided by 3DPLUS and CNES. The pixel size is 5.5 μm . This corresponds to an angular resolution of 0.6 mrad at the center and 0.9 mrad at the edges, hence pixel scales at 1 m of 0.6 mm and 0.9 mm, respectively. The distortion amounts to ~17% on the FOV sides. The spectral response of each camera, integrating the properties of both the detector and the optics, extends approximately from 400 to 800 nanometer. The power consumption amounts to ~1.2 W. Both cameras have been tested in a thermal vacuum chamber with 6 thermal cycles. The electro-optical performances have been measured for the following temperatures: –50°C; –25°C; 0°C; 25°C; 35°C; 50°C (e.g., Fig. 4). For a full description of the cameras, we refer the reader to Th  ret et al. (2024) and Virmon  tois et al. (2024), as they were already present, with the same characteristics, on the Emirate Lunar Mission (ELM) Rashid rover

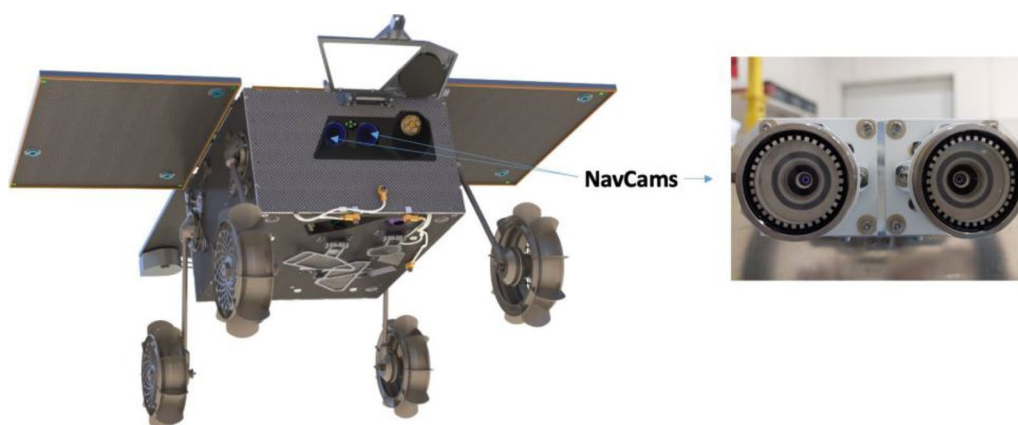


Fig. 1 Overview of the CNES/DLR IDEX rover and its navigation cameras

(Almaeeni et al. 2021). The above scientific investigations and technical objectives require a specific set of calibrations to be carried out. These requirements are specified in the next section.

4 Instrument calibration

The following subsections provide details on the calibrations performed on the NavCams. These included photometry, which links photon count to pixel response; colorimetry, which links detector response to standard human perception; radiometry, which measures the vignetting of the optics and other non-uniformities; and geometry, which reprojects the pixels to a standard/ideal camera for stereo computations.

4.1 Radiometric calibration

4.1.1 Flat fielding

The NavCams proved to be a significant challenge for radiometric calibration due to their very large field of view. The conventional approach to radiometric calibration involves the use of an integrating sphere. However, the large field of view of the cameras was not suited to the limited entrance pupil of the available integrating sphere, leading to a non-uniform illumination across the field of view. Other methods were attempted, including the use of a large television screen and the use of a small diffusive light screen with calibrated luminosity.

Finally, we decided to use a low-particulate, coated paper. In our final setup, the spotlights, which were already behind their own diffusers, were placed behind a sheet of clean room paper held very close to the

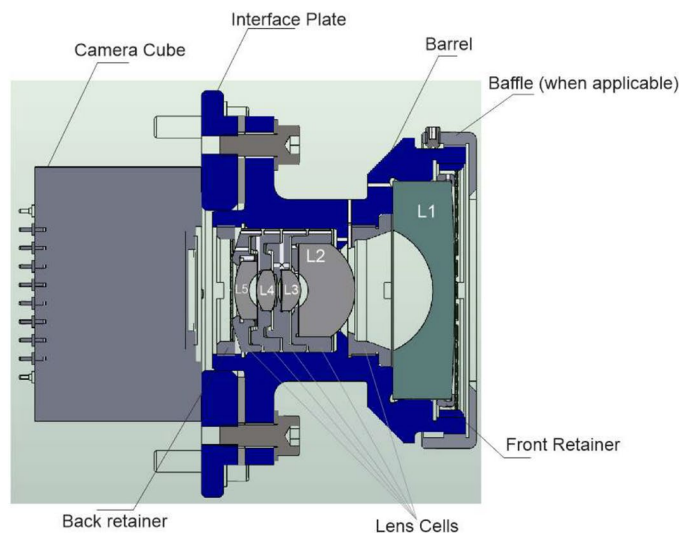
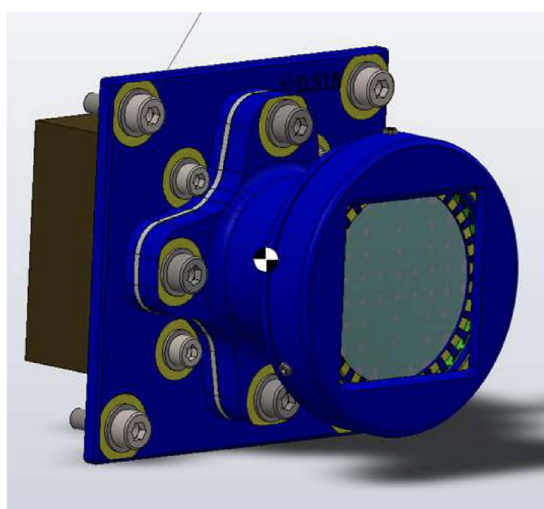


Fig. 2 MMX NavCam overview. (left) Camera definition. (right) Overview of the optical assembly

NavCam stereo bench. The combination of the multiple diffusers ensured that the light was completely uniform to the NavCams. To prevent the majority of reflections, the stereo bench was also concealed behind a black mask, with the lenses remaining concealed. This low cost and highly effective configuration is illustrated in Fig. 5.

It appears that the vignetting is particularly pronounced in the corners, which receive less than 10% of the light at the image's center and deviates from a simple cosine vignetting function (\cos^4). When correcting the images for vignetting, due to the low signal level in the corners, this translates into a loss of signal-to-noise ratio (SNR). However, in the most useful portion of the images, this loss of SNR remains functionally very limited. Furthermore, beyond the pixel-to-pixel response

non-uniformity, it was observed that there is a column-dependent sensitivity bias, which creates vertical stripes in the image at the 2-3% level depending on the integration time.

4.1.2 Colorimetric calibration

A colorimetric characterization of the NavCams was conducted with the objective of providing colorimetric images, that is, images with pixel values that are independent of the sensor, expressed in a standard color space defined by the Commission Internationale de l'Eclairage (CIE). This involves calculating a Color Correction Matrix (CCM) to be applied to the NavCams images that have been previously corrected to remove any deviation from a flat image surface, which is particularly prevalent

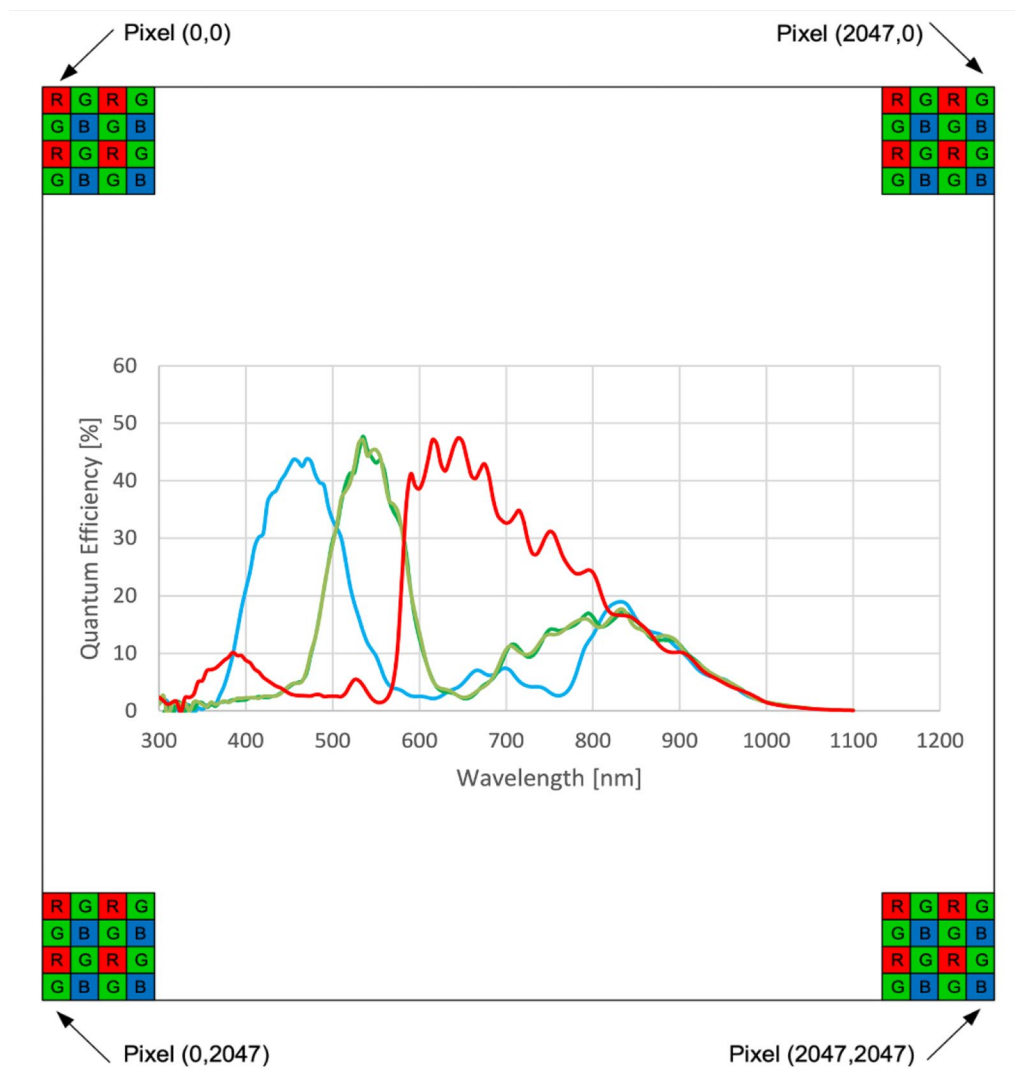


Fig. 3 Illustration of the RGB Bayer pattern order along with their typical spectral response over the bandpass (nm)

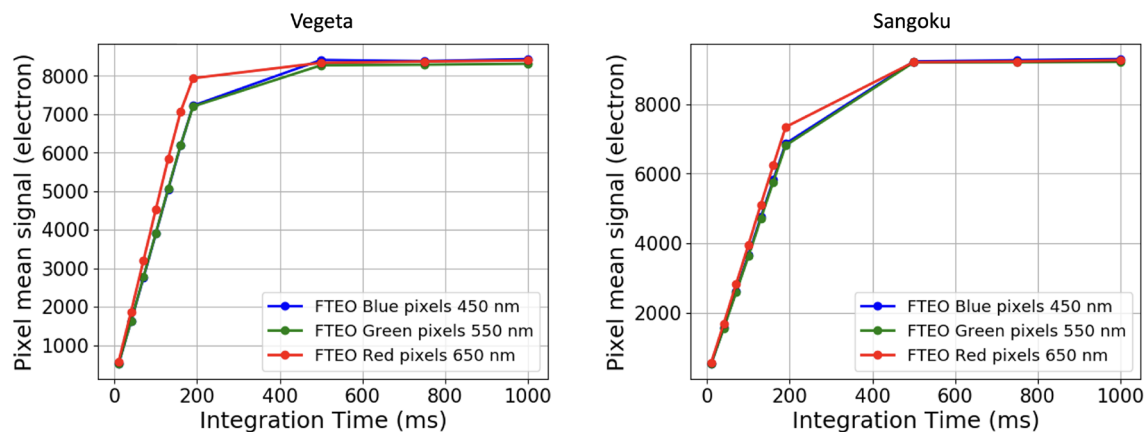


Fig. 4 Electro-optic transfer function of Vegeta (left NavCam) and Sangoku (right NavCam) at 25°C

in images captured using wide-angle optics. The main advantages of this approach are:

- the images can be visualized in colors that are faithful to human perception.
- the images and pixel values can be compared with images acquired by any other camera during any other mission, provided that all images are properly converted to a standard color space.

It is recommended that a Color Correction Matrix (CCM) is calculated in situ (here, at the surface of Phobos) using the image of a color rendition chart comprising a minimum of 24 color patches, as outlined in Alsam and Finlayson (2008). As such a color target could not be accommodated on the rover; the CCM can be estimated if the end-to-end spectral sensitivities of the imaging system are known (measured), as well as the spectral power distribution of the illuminant at Phobos' surface (which is assumed to be similar to that of the Moon). Please refer to Théret et al. (2024) for a detailed description of the method and results.

4.1.3 Absolute calibration

The absolute calibration requires the knowledge of the two parts of the camera: the lens assembly and the image sensor. The design of the lens assembly gives all the required parameters but the spectral transmission. The transmission is characterized by the manufacturer using a two-step method. First, the absolute transmittance is measured at a given wavelength (473nm). The results are obtained by the ratio of the output power with and without the lens. Second, the relative transmittance is measured with a broad spectrum illumination source and a spectrometer. The ratio of the spectrum with and without the lens eliminates any influence from the source.

The measurement is taken on each flight model (left and right). The photon flux on the sensor can be computed for each pixel. However, the sensor only gives the analog-to-digital converter's output (in least significant bit, LSB). First, one must extract the number of photo-generated electrons reaching the photosensitive elements: the external quantum efficiency (EQE). The EQE is taken from the sensor datasheet verified by additional measurements. It takes into account the complete optical stack (protection window, color filters, microlenses) and the electrical architecture (epi-layer depth, pixel design). The photon transfer curve (PTC) plots the variance versus the mean signal. The linear region slope gives the total conversion factor (CVF) in LSB/e-. The two flight models were measured under illumination at three wavelengths



Fig. 5 Radiometric calibration with AIT paper



Fig. 6 Geometric calibration with a small checkerboard

and multiple temperatures. The CVF changes slightly depending on the camera, but remains constant with the wavelength and the temperature.

4.2 Geometric calibration

To perform the geometric calibration, a 7x10 checkerboard was placed in different positions. These positions were specifically designed to try and obtain as much information as possible from the side's and corner's deformations. The positions of the checkerboard were designed in such a way that the closest intersection between the squares was separated from the edge of the image by a distance of between 25 and 30 pixels. An example of this type of image is shown in Fig. 6.

Ultimately, using OpenCV 4.5.5 to the available data resulted in the generation of an “r4t2” model with four radial (r), two tangential (t) and four thin-prism (P) coefficients of the distortion model:

$$\begin{pmatrix} x' \\ y' \end{pmatrix} = \begin{pmatrix} x \cdot \frac{1+r_1d^2+r_2d^4+r_3d^6}{1+r_4d^2+r_5d^4+r_6d^6} + 2t_1xy + t_2(d^2+2x^2) + p_1d^2 + p_2d^4 \\ y \cdot \frac{1+r_1d^2+r_2d^4+r_3d^6}{1+r_4d^2+r_5d^4+r_6d^6} + t_1(d^2+2y^2) + 2t_2xy + p_3d^2 + p_4d^4 \end{pmatrix}$$

where $d^2 = x^2 + y^2$

The optimal model identified was the r4t2 model without thin-prism coefficients, which yielded a reprojection error RMS of 0.24 pixels.¹

5 Data processing pipeline

A scientific pipeline is currently being developed to process the raw NavCam data and generate high-level science products. This pipeline, developed in Python, benefits from a heritage from the Rosetta mission.

The pipeline aims to generate:

- Radiometrically and geometrically calibrated stereo pairs
- 3D digital terrain models (DTMs) of the observed scenes
- Albedo and color maps
- Low-resolution spectral maps
- Maps of gravitational heights and slopes

The four principal processing steps are as follows:

- Step 1: Preprocessing of the images to obtain radiometrically and geometrically calibrated images using the laboratory and in-flight calibration data. This includes the detection of saturated/bad pixels, correction from bias/flat/dark, application of the absolute calibration factor, debayering and geometric correction (e.g., Fig. 7).
- Step 2: Calculation of color ratios, spectral slopes and search for an absorption band in the red filter. This requires, among others, the identification of the images sharing a common fraction of field of view and the subsequent alignment of these images based on the identification of points of interest.
- Step 3: Calculation of digital terrain models (DTMs). The Agisoft metashape software (e.g., Rahman and Cahyono (2023)) will be used to produce a first DTM using a stereo pair (e.g., Fig. 8). This approach requires knowledge of the camera-surface distance at the center of the field of view. Points of interest will be used to determine this distance. The second step will involve the utilization of the Multi-resolution PhotoClinometry by Deformation (MPCD) method (Capanna et al. 2013; Jorda et al. 2016) to refine the initial DTM. This method involves gradually deforming the vertices of an initial mesh to minimize the difference between the observed images and synthetic images of the deformed model created with the OASIS software (Optimised Astrophysical Simulator for Imaging Systems; Jorda et al. 2010). The OASIS software employs a shape model described by a triangular mesh in conjunction with geometric and radiometric parameters in order to generate realistic images of the surface. As inputs, this software takes the position and orientation of the target in the camera frame, the radiometric properties of the

¹ This represents an error of less than 0.12 pixels during the operations because a 2x2 binning will be applied during readout.

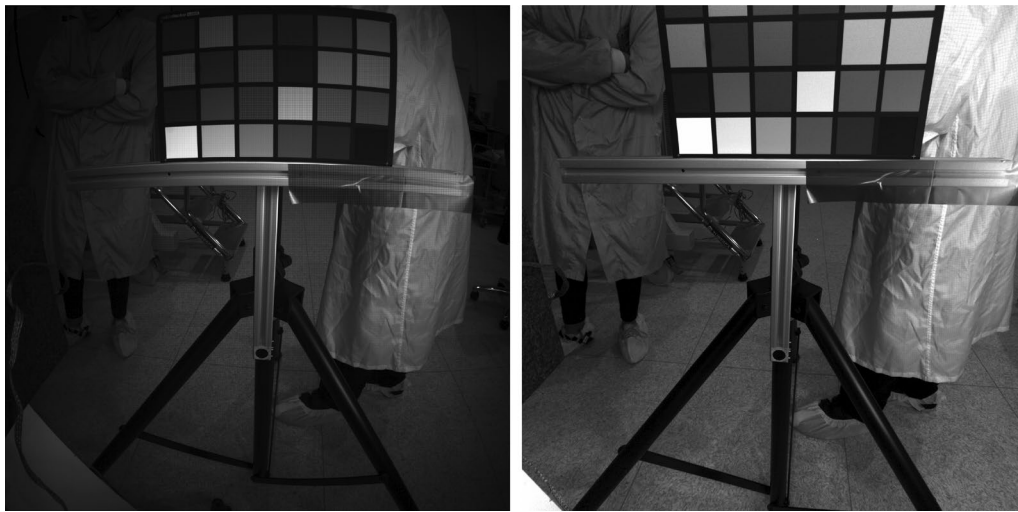


Fig. 7 Before (left) and after (right) preliminary radiometric and geometric calibration

camera, the rotational parameter of the object, and the reflectance properties of its surface. The MPCD method has already been successfully applied to images of small bodies observed by the Rosetta mission, notably those of comet 67P (Jorda et al. 2016). It is crucial to emphasize that the MPCD method requires the acquisition of at least five images with varying incident angles to ensure the generation of a reliable and accurate digital terrain model (DTM).

- Step 4: Calculation of georeferenced maps of physical parameters. The 3D model, in conjunction with the geometric data retrieved in Step 3, will be employed to project spectral slopes and albedos onto the DTM and to generate the corresponding GIS products. Additionally, gravitational parameters associated with the DTMs (dynamic heights and slopes) will be calculated using the global shape model produced by the TENG00, OROCHI and LIDAR observations.

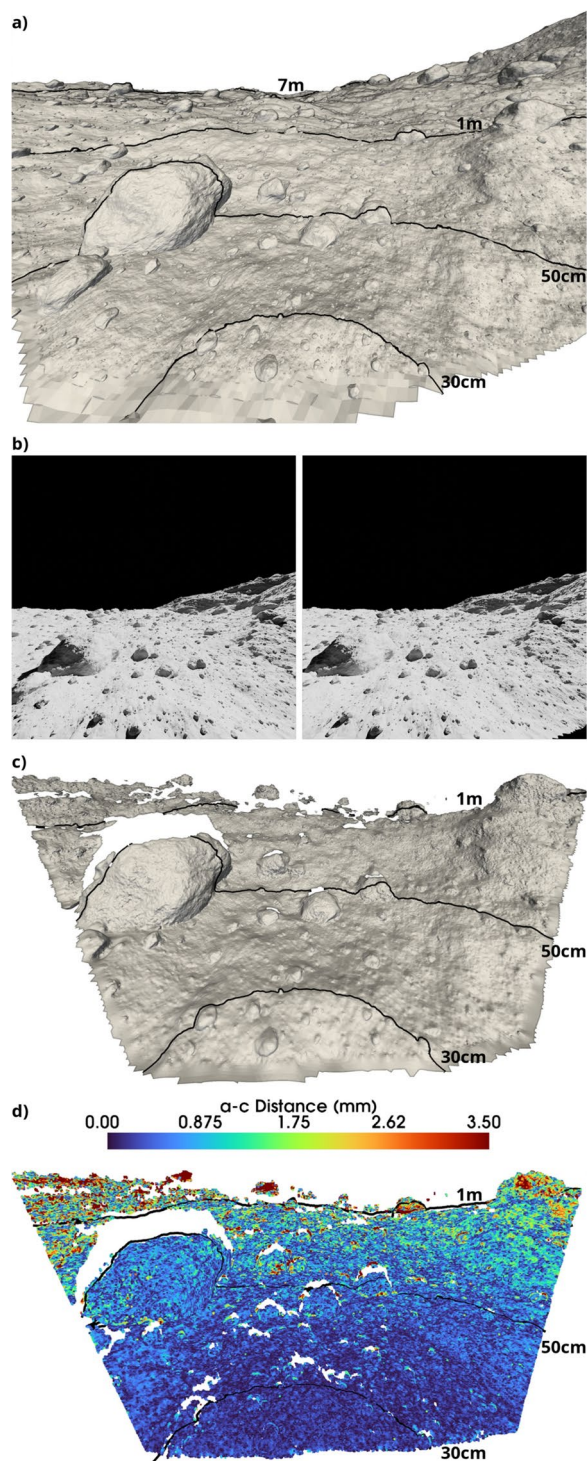
To develop and test the pipeline, we have developed a simulator that generates realistic stereo pairs of Phobos' surface (Fig. 8). It is based on fractal subdivisions of local areas extracted from the global shape model of Phobos (Ernst et al. 2023). Random shape boulders with a random power-law size distribution are added to the local shape model. The rendering is performed with the Blender software (Hess 2010; Community 2018).

6 Observation strategy and operations

The NavCams represent the inaugural instrument to be used on IDEFIX, starting image acquisition even before landing. A series of images will be acquired during the SLUD (Separation, Landing, Uprighting and Deployment) sequence. The sequence starts before the separation, intending to capture an image of Phobos, possibly including Mars. Image acquisition continues as the rover descends from an altitude of approximately 40 m, following its separation from the MMX spacecraft. Some of these images may be retrieved in a heavily binned or compressed form before the spacecraft loses communication with the rover. During the rover's bounces, the integration time will be reduced in an attempt to minimize the effects of motion blur. Finally, the NavCams will be activated during the uprighting sequence, as the rover pivots to its belly and stands up on its legs. The majority of these images will be monocular due to the constraints of limited bandwidth.

Subsequently, the NavCams will be used as the principal sensor of the rover for contextual information. The initial image captured following the rover's uprighting will be used for the localization of the rover at the surface of Phobos, within an uncertainty ellipse of up to 100 m in diameter. NavCam images will be acquired before and after each displacement. Context images will be given priority in all science telemetry.

The NavCams will be an essential sensor for the two autonomous navigation software programs (from CNES



and DLR) that are being tested on the IDEFIX rover. For context and navigation purposes, the images will be binned 2x2 and the color information will be lost. However, for scientific purposes (see section 2), full-frame

◀ **Fig. 8** DTM reconstruction from synthetic images. **a** Original DTM used to create the synthetic images. We used the most recent 3D shape model of Phobos (Ernst et al. 2023) on which boulders were locally added. **b** Realistic stereo pair of NavCam images. These synthetic images were produced using the parameters of the camera (focal length, field of view, pixel scale, position above the surface, etc.) as well as the starting DTM shown in (a). Rendering was done with the Blender software. **c** DTM reconstructed with the Agisoft metashape software using the stereo pair (b) as input. **d** Distance map computed as a–c representing an estimate of the error which is typically less than 1 mm within the first meter

2048x2048 images, monocular and/or stereo, will also be acquired.

A final observation that will be attempted is the imaging of levitating dust at dusk. This phenomenon has been observed on the Moon, and it has been hypothesized that it also occurs on small bodies like asteroids. At night, the NavCams will take long exposure images with the four white LEDs switched on to ascertain whether any discernible phenomenon becomes visible at night.

7 Conclusions

The CNES/DLR IDEFIX rover of the JAXA MMX mission is scheduled to be delivered to the surface of Phobos on the anti-Mars side in December 2028. The goal of the rover is to travel across the surface of Phobos for at least 100 days, with autonomous guidance provided by the NavCams. During this expedition, the first of its kind on a low-gravity body, the images collected by the NavCams will provide elements of answers to a number of scientific questions, including but not limited to the origin of the color dichotomy and the nature of space weathering processes on Phobos. Ground calibrations of the NavCams performed at CNES (Toulouse) have shown that all scientific requirements will be met. A processing pipeline is currently being developed at the Laboratoire d'Astrophysique de Marseille to transform the raw NavCam data into high-level science products.

Abbreviations

JAXA: Japan Aerospace eXploration Agency

Acknowledgements

PV, LJ, OG and AP acknowledge support from CNES.

Author contributions

S.T., J.B., E.R., J.B., V.L., E.R., N.T., and C.V. were responsible for the delivery and calibration of the navigation cameras and provided a description of this activity for the manuscript. P.M. & S.U. are responsible for the management of the rover activities. P.V. leads the science activity of the navigation cameras and led the writing of the manuscript. P.V., L.J., C.P., A.P., O.G. and P-Y.C. are in charge of the development of the scientific pipeline. N.M., S.L.M., P.B., O.R., J.F., S.C., J.L., M.A.B. and A.D. provided scientific contributions to the paper.

Funding

This work was supported by CNES.

Availability of data and materials

Not applicable.

Declarations

Competing interests

The authors declare that they have no conflict of interest.

Received: 18 October 2024 Accepted: 27 April 2025

Published online: 01 July 2025

References

- Almaeenei S, Els SG, Almarzooqi H (2021) To a Dusty Moon: Rashid's Mission to Observe Lunar Surface Processes Close-Up. *Lunar Planet Sci Conf* 2548:1906
- Alsam A, Finlayson G (2008) Integer programming for optimal reduction of calibration targets. *Color Res Appl: Endorsed Inter-Soc Color Counc, Colour Group (Great Britain), Can Soc Color, Color Sci Assoc Japan, Dutch Soc Study Color, Swedish Colour Centre Foundat, Colour Soc Austr, Centre Français de la Couleur* 33(3):212–220
- Barucci MA, Reess J-M, Bernardi P, Doressoundiram A, Fornasier S, Le Du M, Iwata T, Nakagawa H, Nakamura T, André Y, Aoki S, Arai T, Baldi E, Beck P, Buey J-T, Canalias E, Castelnau M, Charnoz S, Chaussidon M, Chapron F, Ciarletti V, Delbo M, Dubois B, Gauffre S, Gautier T, Genda H, Hassen-Khodja R, Hervet G, Hyodo R, Imbert C, Imamura T, Jorda L, Kameda S, Kouach D, Kouyama T, Kuroda T, Kurokawa H, Lapaw L, Lasue J, Le Deit L, Ledot A, Leyrat C, Le Ruyet B, Matsuoka M, Merlin F, Miyamoto H, Moynier F, Nguyen Tuong N, Ogohara K, Osawa T, Parisot J, Pistre L, Quartier B, Raymond SN, Rocard F, Sakanai T, Sato TM, Sawyer E, Tache F, Trémolières S, Tsuchiya F, Vernazza P, Zeganadin D (2021) MIRS: an imaging spectrometer for the MMX mission. *Earth, Planets Space* 73(1):211. <https://doi.org/10.1186/s40623-021-01423-2>
- Basilevsky AT, Head JW, Horz F, Ramsley K (2015) Survival times of meter-sized rock boulders on the surface of airless bodies. *Planet Space Sci* 117:312–328. <https://doi.org/10.1016/j.pss.2015.07.003>
- Bigot J, Lombardo P, Murdoch N, Scheeres DJ, Vivet D, Zhang Y, Sunshine J, Vincent JB, Barnouin OS, Ernst CM, Daly RT, Sunday C, Michel P, Campo-Bagatin A, Lucchetti A, Pajola M, Rivkin AS, Chabot NL (2024) The bearing capacity of asteroid (65803) Didymos estimated from boulder tracks. *Nat Commun* 15:6204. <https://doi.org/10.1038/s41467-024-50149-8>
- Brunetto R, Loeffler MJ, Nesvorný D, Sasaki S, Strazzulla G (2015) Asteroid Surface Alteration by Space Weathering Processes. *Asteroids IV*. https://doi.org/10.2458/azu_uapress_9780816532131-ch031
- Canup R, Salmon J (2018) Origin of Phobos and Deimos by the impact of a Vesta-to-Ceres sized body with Mars. *Sci Adv* 4(4):6887. <https://doi.org/10.1126/sciadv.aar6887>
- Capanna C, Gesquiere G, Jorda L, Lamy P, Vibert D (2013) Three-dimensional reconstruction using multiresolution photogrammetry by deformation. *Vis Comput* 29:825–835. <https://doi.org/10.1007/s00371-013-0821-5>
- Colwell JE, Gulbis A, Horányi M, Robertson S (2005) Dust transport in photoelectron layers and the formation of dust ponds on Eros. *Icarus* 175(1):159–169. <https://doi.org/10.1016/j.icarus.2004.11.001>
- Blender OC (2018) Blender—A 3D modelling and rendering package. *Retrieval Rep Seq Constr* 4:128
- Criswell DR (1973) Horizon-glow and the motion of lunar dust photon and particle interactions with surfaces in space. *Astrophys Space Sci Library*. https://doi.org/10.1007/978-94-010-2647-5_36
- DellaGiustina DN, Kaplan HH, Simon AA, Bottke WF, Avdellidou C, Delbo M, Ballouz R-L, Golish DR, Walsh KJ, Popescu M, Campins H, Barucci MA, Poggiali G, Daly RT, Le Corre L, Hamilton VE, Porter N, Jawin ER, McCoy TJ, Connolly HC, García J, Tatsumi E, de Leon J, Licandro J, Fornasier S, Daly MG, Al Asad MM, Philpott L, Seabrook J, Barnouin OS, Clark BE, Nolan MC, Howell ES, Binzel RP, Rizk B, Reuter DC, Lauretta DS (2021) Exogenic basalt on asteroid (101955) Bennu. *Nature Astron* 5:31–38. <https://doi.org/10.1038/s41550-020-1195-z>
- Duxbury TC, Zakharov AV, Hoffmann H, Guinness EA (2014) Spacecraft exploration of Phobos and Deimos. *Planet Space Sci* 102:9–17. <https://doi.org/10.1016/j.pss.2013.12.008>
- Eppes M-C, Willis A, Molaro J, Abernathy S, Zhou B (2015) Cracks in Martian boulders exhibit preferred orientations that point to solar-induced thermal stress. *Nat Commun* 6:6712. <https://doi.org/10.1038/ncomms7712>
- Ernst CM, Daly RT, Gaskell RW, Barnouin OS, Nair H, Hyatt BA, Al Asad MM, Hoch K (2023) High-resolution shape models of Phobos and Deimos from stereophotoclinometry. *Earth, Planets Space* 75(1):103. <https://doi.org/10.1186/s40623-023-01814-7>
- Golish DR, DellaGiustina DN, Li JY, Clark BE, Zou XD, Smith PH, Rizos JL, Hasselmann PH, Bennett CA, Fornasier S, Ballouz RL (2021) Disk-resolved photometric modeling and properties of asteroid (101955) Bennu. *Icarus* 357:113724
- Gradie J, Veverka J (1986) The wavelength dependence of phase coefficients. *Icarus* 66(3):455–467. [https://doi.org/10.1016/0019-1035\(86\)90085-0](https://doi.org/10.1016/0019-1035(86)90085-0)
- Hapke B (2012) *Theory of Reflectance and Emittance Spectroscopy*. Cambridge University Press. <https://doi.org/10.1017/CBO9781139025683>
- Hess R (2010) *Blender Foundations: The Essential Guide to Learning Blender 2.6*. Focal Press
- Hörz F, Basilevsky AT, Head JW, Cintala MJ (2020) Erosion of lunar surface rocks by impact processes: a synthesis. *Planet Space Sci* 194:105105. <https://doi.org/10.1016/j.pss.2020.105105>
- Hyodo R, Genda H, Charnoz S, Rosenblatt P (2017) On the impact origin of phobos and deimos. I. thermodynamic and physical aspects. *Astrophys J* 845(2):125. <https://doi.org/10.3847/1538-4357/aa81c4>. [arXiv:1707.06282](https://arxiv.org/abs/1707.06282)
- Hyodo R, Kurosawa K, Genda H, Usui T, Fujita K (2019) Transport of impact ejecta from Mars to its moons as a means to reveal Martian history. *Sci Rep* 9:19833. <https://doi.org/10.1038/s41598-019-56139-x>. [arXiv:1912.12056](https://arxiv.org/abs/1912.12056)
- Hyodo R, Genda H, Sekiguchi R, Madeira G, Charnoz S (2022) Challenges in forming phobos and deimos directly from a splitting of an ancestral single moon. *Planet Sci J* 3(8):204. <https://doi.org/10.3847/PSJ/ac88d2>. [arXiv:2208.04794](https://arxiv.org/abs/2208.04794)
- Jaumann R, Schmitz N, Ho T-M, Schröder SE, Otto KA, Stephan K, Elgner S, Krohn K, Preusker F, Scholten F, Biele J, Ullamec S, Krause C, Sugita S, Matz K-D, Roatsch T, Parekh R, Mottola S, Grott M, Michel P, Trauthan F, Koncz A, Michaelis H, Lange C, Grundmann JT, Maibaum M, Sasaki K, Wolff F, Reill J, Moussi-Soffys A, Lorda L, Neumann W, Vincent J-B, Wagner R, Bibring J-P, Kameda S, Yano H, Watanabe S, Yoshikawa M, Tsuda Y, Okada T, Yoshimitsu T, Mimasu Y, Saiki T, Yabuta H, Rauer H, Honda R, Morota T, Yokota Y, Kouyama T (2019) Images from the surface of asteroid Ryugu show rocks similar to carbonaceous chondrite meteorites. *Science* 365(6455):817–820. <https://doi.org/10.1126/science.aaw8627>
- Jin W, Zhang H, Yuan Y, Yang Y, Shkuratov YG, Lucey PG, Kaydash VG, Zhu M-H, Xue B, Di K, Xu B, Wan W, Xiao L, Wang Z (2015) In situ optical measurements of Chang'E-3 landing site in Mare Imbrium: 2. Photometric properties of the regolith. *Geophys Res Lett* 42(20):8312–8319. <https://doi.org/10.1002/2015GL065789>
- Johnson JR, Grundy WM, Lemmon MT, Bell JF, Johnson MJ, Deen RG, Arvidson RE, Farrand WH, Guinness EA, Hayes AG, Herkenhoff KE, Seelos F, Soderblom J, Squyres S (2006) Spectrophotometric properties of materials observed by Pancam on the Mars Exploration Rovers: 1. Spirit. *J Geophys Res (Planets)* 111(E2):02–14. <https://doi.org/10.1029/2005JE002494>
- Johnson JR, Grundy WM, Lemmon MT, Bell JF, Johnson MJ, Deen R, Arvidson RE, Farrand WH, Guinness E, Hayes AG, Herkenhoff KE, Seelos F, Soderblom J, Squyres S (2006) Spectrophotometric properties of materials observed by Pancam on the Mars Exploration Rovers: 2. Opportunity. *J Geophys Res (Planets)* 111(E12):12–16. <https://doi.org/10.1029/2006JF002762>
- Johnson JR, Grundy WM, Lemmon MT, Bell JF, Deen RG (2015) Spectrophotometric properties of materials observed by Pancam on the Mars Exploration Rovers: 3. Sols 500–1525. *Icarus* 248:25–71. <https://doi.org/10.1016/j.icarus.2014.10.026>
- Johnson JR, Grundy WM, Lemmon MT, Liang W, Bell JF, Hayes AG, Deen RG (2021) Spectrophotometric properties of materials observed by Pancam on the Mars Exploration Rovers: 4. Final mission observations. *Icarus* 357:114261. <https://doi.org/10.1016/j.icarus.2020.114261>

- Johnson JR, Grundy WM, Lemmon MT, Liang W, Bell JF, Hayes AG, Deen RG (2022) Spectrophotometric properties of materials from the Mars Science Laboratory at Gale crater: 1. Bradbury Landing to Cooperstown. *Planet Space Sci* 222:105563. <https://doi.org/10.1016/j.pss.2022.105563>
- Jorda L, Spjuth S, Keller HU, Lamy P, Llebaria A (2010) OASIS: a simulator to prepare and interpret remote imaging of solar system bodies. In: Bouman, C.A, Pollak, I, Wolfe, P.J (eds.) *Computational Imaging VIII*. Society of Photo-Optical Instrumentation Engineers (SPIE) Conference Series, vol 7533, p 753311. <https://doi.org/10.1117/12.838893>
- Jorda L et al (2016) The global shape, density and rotation of Comet 67P/Churyumov-Gerasimenko from preperihelion Rosetta/OSIRIS observations. *Icarus*. 277:257–278
- Kameda S, Ozaki M, Enya K, Fuse R, Kouyama T, Sakatani N, Suzuki H, Osada N, Kato H, Miyamoto H, Yamazaki A, Nakamura T, Okamoto T, Ishimaru T, Hong P, Ishibashi K, Takashima T, Ishigami R, Kuo C-L, Abe S, Goda Y, Murao H, Fujishima S, Aoyama T, Hagiwara K, Mizumoto S, Tanaka N, Murakami K, Matsumoto M, Tanaka K, Sakuta H (2021) Design of telescopic nadir imager for geomorphology (TENGOO) and observation of surface reflectance by optical chromatic imager (OROCHI) for the Martian Moons Exploration (MMX). *Earth, Planets Space* 73(1):218. <https://doi.org/10.1186/s40623-021-01462-9>
- Kawakatsu Y, Kuramoto K, Usui T, Sugahara H, Ootake H, Yasumitsu R, Yoshikawa K, Mary S, Grebenstein M, Sawada H, Imada T, Shimada T, Ogawa K, Otsuki M, Baba M, Fujita K, Zacny K, van Dyne D, Satoh Y, Tokaji A (2023) Preliminary design of Martian Moons eXploration (MMX). *Acta Astronaut* 202:715–728. <https://doi.org/10.1016/j.actaastro.2022.09.009>
- Kuramoto K, Kawakatsu Y, Fujimoto M, Araya A, Barucci MA, Genda H, Hirata N, Ikeda H, Imamura T, Helbert J, Kameda S, Kobayashi M, Kusano H, Lawrence DJ, Matsumoto K, Michel P, Miyamoto H, Morota T, Nakagawa H, Nakamura T, Ogawa K, Otake H, Ozaki M, Russell S, Sasaki S, Sawada H, Senshu H, Tachibana S, Terada N, Ulamec S, Usui T, Wada K, Watanabe S, Yokota S (2022) Martian moons exploration MMX: sample return mission to Phobos elucidating formation processes of habitable planets. *Earth, Planets Space* 74(1):12. <https://doi.org/10.1186/s40623-021-01545-7>
- ...La Forgia F, Giacomini L, Lazzarin M, Massironi M, Oklay N, Scholten F, Pajola M, Bertini I, Cremonese G, Barbieri C, Naletto G, Simioni E, Preusker F, Thomas N, Sierks H, Lamy P, Rodrigo R, Koschny D, Rickman H, Keller HU, Agarwal J, Auger A-T, A'Hearn MF, Barucci MA, Bertaux J-L, Besse S, Bodevits D, Da Deppo V, Davidsson B, Debei S, De Cecco M, El-Maarry MR, Ferri F, Fornasier S, Fulle M, Groussin O, Gutiérrez PJ, Güttler C, Hall I, Hviid SF, Ip W-H, Jorda L, Knollenberg J, Kramm JR, Kürt E, Küppers M, Lara L-M, Lopez Moreno JJ, Magrin S, Marzari F, Michalik H, Mottola S, Pommerol A, Tubiana C, Vincent J-B (2015) Geomorphology and spectrophotometry of Philae's landing site on comet 67P/Churyumov-Gerasimenko. *Astron Astrophys* 583:41. <https://doi.org/10.1051/0004-6361/201525983>
- Lantz C, Binzel RP, DeMeo FE (2018) Space weathering trends on carbonaceous asteroids: a possible explanation for Bennu's blue slope? *Icarus* 302:10–17. <https://doi.org/10.1016/j.icarus.2017.11.010>
- Lederer SM, Domingue DL, Vilas F, Abe M, Farnham TL, Jarvis KS, Lowry SC, Ohba Y, Weissman PR, French LM, Fukai H, Hasegawa S, Ishiguro M, Larson SM, Takagi Y (2005) Physical characteristics of Hayabusa target Asteroid 25143 Itokawa. *Icarus* 173(1):153–165. <https://doi.org/10.1016/j.icarus.2004.07.022>
- Lin H, Xu R, Yang W, Lin Y, Wei Y, Hu S, He Z, Qiao L, Wan W (2020) In situ photometric experiment of lunar regolith with visible and near-infrared imaging spectrometer on board the yutu-2 lunar rover. *J Geophys Res(Planets)* 125(2):06076. <https://doi.org/10.1029/2019JE006076>
- Mahlke M, Carry B, Mattei P-A (2022) Asteroid taxonomy from cluster analysis of spectrometry and albedo. *Astron Astrophys* 665:26. <https://doi.org/10.1051/0004-6361/202243587>. [arXiv:2203.11229](https://arxiv.org/abs/2203.11229)
- ...McCord TB, Li J-Y, Combe J-P, McSweeney HY, Jaumann R, Reddy V, Tosi F, Williams DA, Blewett DT, Turrini D, Palomba E, Pieters CM, de Sanctis MC, Ammannito E, Capria MT, Le Corre L, Longobardo A, Nathues A, Mittlefehldt DW, Schröder SE, Hiesinger H, Beck AW, Capaccioni F, Carsenty U, Keller HU, Denevi BW, Sunshine JM, Raymond CA, Russell CT (2012) Dark material on Vesta from the infall of carbonaceous volatile-rich material. *Nature* 491(7422):83–86. <https://doi.org/10.1038/nature11561>
- McFadden LD, Eppes MC, Gillespie AR, Hallet B (2005) Physical weathering in arid landscapes due to diurnal variation in the direction of solar heating. *Geol Soc Am Bull* 117(1):161. <https://doi.org/10.1130/B25508.1>
- Michel P, Ulamec S, Böttger U, Grott M, Murdoch N, Vernazza P, Sunday C, Zhang Y, Valette R, Castellani R, Biele J, Tardivel S, Groussin O, Jorda L, Knollenberg J, Grundmann JT, Arrat D, Pont G, Mary S, Grebenstein M, Miyamoto H, Nakamura T, Wada K, Yoshikawa K, Kuramoto K (2022) The MMX rover: performing in situ surface investigations on Phobos. *Earth, Planets Space* 74(1):2. <https://doi.org/10.1186/s40623-021-01464-7>
- Molaro JL, Hergenrother CW, Chesley SR, Walsh KJ, Hanna RD, Haberle CW, Schwartz SR, Ballouz R-L, Bottke WF, Campins HJ, Lauretta DS (2020) Thermal fatigue as a driving mechanism for activity on asteroid bennu. *J Geophys Res(Planets)* 125(8):06325. <https://doi.org/10.1029/2019JE006325>. <https://doi.org/10.1002/essoar.10501385.2>
- Murchie SL, Britt DT, Head JW, Pratt SF, Fisher PC, Zhukov BS, Kuzmin AA, Ksanfomaloty LV, Zharkov AV, Nikitin GE, Fanale FP, Blaney DL, Bell JF, Robinson MS (1991) Color heterogeneity of the surface of Phobos: relationships to geologic features and comparison to meteorite analogs. *J Geophys Res: Solid Earth* 96:5925–5945. <https://doi.org/10.1029/90JB02354>
- Murchie S, Erard S (1996) Spectral properties and heterogeneity of PHOBOS from measurements by PHOBOS 2. *Icarus* 123(1):63–86. <https://doi.org/10.1006/icar.1996.0142>
- ...Otto KA, Matz K-D, Schröder SE, Parekh R, Krohn K, Honda R, Kameda S, Jaumann R, Schmitz N, Stephan K, Sugita S, Tatsumi E, Ho T-M, Koncz A, Trauth F, Cho Y, Hayakawa M, Honda C, Kouyama T, Matsuoaka M, Morota T, Mottola S, Ogawa K, Preusker F, Sakatani N, Sawada H, Scholten F, Suzuki H, Yamada M, Yokota Y, Yoshioka K (2021) Surface roughness of asteroid (162173) Ryugu and comet 67P/Churyumov-Gerasimenko inferred from in situ observations. *Monthly Notices Royal Astron Soc* 500(3):3178–3193. <https://doi.org/10.1093/mnras/staa3314>
- Otto K, Ho T-M, Ulamec S, Bibring J-P, Biele J, Grott M, Hamm M, Hercik D, Jaumann R, Sato M, Schröder SE, Tanaka S, Auster U, Kitazato K, Knollenberg J, Moussi A, Nakamura T, Okada T, Pilorget C, Schmitz N, Sugita S, Wada K, Yabuta H (2023) MASCOt's in situ analysis of asteroid Ryugu in the context of regolith samples and remote sensing data returned by Hayabusa2. *Earth, Planets Space* 75(1):51. <https://doi.org/10.1186/s40623-023-01805-8>
- Patzek M, Rüschoff O (2022) Experimentally induced thermal fatigue on lunar and eucrite meteorites—influence of the mineralogy on rock breakdown. *J Geophys Res(Planets)* 127(10):2022–007306. <https://doi.org/10.1029/2022JE007306>
- Pieters CM, Ammannito E, Blewett DT, Denevi BW, De Sanctis MC, Gaffey MJ, Le Corre L, Li J-Y, Marchi S, McCord TB, McFadden LA, Mittlefehldt DW, Nathues A, Palmer E, Reddy V, Raymond CA, Russell CT (2012) Distinctive space weathering on Vesta from regolith mixing processes. *Nature* 491(7422):79–82. <https://doi.org/10.1038/nature11534>
- Pieters CM, Noble SK (2016) Space weathering on airless bodies. *J Geophys Res(Planets)* 121(10):1865–1884. <https://doi.org/10.1002/2016JE005128>
- Piquette M, Horányi M (2017) The effect of asymmetric surface topography on dust dynamics on airless bodies. *Icarus* 291:65–74. <https://doi.org/10.1016/j.icarus.2017.03.019>
- Rahman A, Cahyono AB (2023) Analysis of 3-d building modeling using photogrammetric software: Agisoft metashape and micmac. *IOP Conf Ser: Earth Environ Sci* 1276(1):012044. <https://doi.org/10.1088/1755-1315/1276/1/012044>
- Ramsley KR, Head JW (2013) Mars impact ejecta in the regolith of Phobos: Bulk concentration and distribution. *Planets* 87:115–129. <https://doi.org/10.1016/j.pss.2013.09.005>
- Reddy V, Le Corre L, O'Brien DP, Nathues A, Cloutis EA, Durda DD, Bottke WF, Bhatt MU, Nesvorniy D, Buczkowski D, Scully J, Palmer EM, Sierks H, Mann PJ, Becker KJ, Beck AW, Mittlefehldt D, Li J-Y, Gaskell R, Russell CT, Gaffey MJ, McSweeney HY, McCord TB, Combe J-P, Blewett D (2012) Delivery of dark material to Vesta via carbonaceous chondritic impacts. *Icarus* 221(2):544–559. <https://doi.org/10.1016/j.icarus.2012.08.011>. [arXiv:1208.2833](https://arxiv.org/abs/1208.2833)
- Rennilson JJ, Criswell DR (1974) Surveyor Observations of Lunar Horizon-Glow. *Moon* 10(2):121–142. <https://doi.org/10.1007/BF00655715>
- Ronnet T, Vernazza P, Mousis O, Brugger B, Beck P, Devouard B, Witasse O, Cipriani F (2016) Reconciling the orbital and physical properties of the martian moons. *Astrophys J* 828(2):109. <https://doi.org/10.3847/0004-637X/828/2/109>. [arXiv:1607.02350](https://arxiv.org/abs/1607.02350)
- Rosenblatt P, Charnoz S, Dunseath KM, Terao-Dunseath M, Trinh A, Hyodo R, Genda H, Toupin S (2016) Accretion of Phobos and Deimos in an

- extended debris disc stirred by transient moons. *Nat Geosci* 9(8):581–583. <https://doi.org/10.1038/ngeo2742>
- Ruesch O, Sefton-Nash E, Vago JL, Küppers M, Pasckert JH, Krohn K, Otto K (2020) In situ fragmentation of lunar blocks and implications for impacts and solar-induced thermal stresses. *Icarus* 336:113431. <https://doi.org/10.1016/j.icarus.2019.113431>
- Rüsch O, Wöhler C (2022) Degradation of rocks on the Moon: Insights on abrasion from topographic diffusion LRO/NAC and Apollo images. *Icarus* 384:115088. <https://doi.org/10.1016/j.icarus.2022.115088>
- Rüsch O, Bickel VT (2023) Global mapping of fragmented rocks on the moon with a neural network: implications for the failure mode of rocks on airless surfaces. *Planet Sci J* 4(7):126. <https://doi.org/10.3847/PSJ/acd1ef>
- Rüsch O, Hess M, Wöhler C, Bickel VT, Marshal RM, Patzek M, Huybrighs H (2024) Discovery of a dust sorting process on boulders near the reiner gamma swirl on the moon. *J Geophys Res(Planets)* 129(1):2023–007910. <https://doi.org/10.1029/2023JE007910>
- Sasaki S, Kanda S, Kikuchi H, Michikami T, Morota T, Honda C, Miyamoto H, Henmi R, Sugita S, Tatsumi E, Kanamaru M, Watanabe S, Namiki N, Michel P, Hirabayashi M, Hirata N, Nakamura T, Noguchi T, Hiroi T, Matsumoto K, Sakatani N, Kameda S, Kouyama T, Suzuki H, Yamada M, Honda R, Cho Y, Yoshioka K, Hayakawa M, Matsuoka M, Noguchi R, Sawada H, Yokota Y, Yoshikawa M (2021) Crack orientations of boulders on ryugu: N-S preference and exfoliation feature. *Lunar Planet Sci Conf* 2548:2010
- Schirner L, Otto KA, Delbo M, Matz KD, Sasaki S, Sugita S (2024) Aligned fractures on asteroid Ryugu as an indicator of thermal fracturing. *Astron Astrophys* 684:A5
- Tatsumi E, Domingue D, Schröder S, Yokota Y, Kuroda D, Ishiguro M, Hasegawa S, Hiroi T, Honda R, Hemmi R, Le Corre L, Sakatani N, Morota T, Yamada M, Kameda S, Kouyama T, Suzuki H, Cho Y, Yoshioka K, Matsuoka M, Honda C, Hayakawa M, Hirata N, Hirata N, Yamamoto Y, Vilas F, Takato N, Yoshikawa M, Abe M, Sugita S (2020) Global photometric properties of (162173) Ryugu. *Astron Astrophys* 639:A83. <https://doi.org/10.1051/0004-6361/201937096>
- Tatsumi E, Sugimoto C, Riu L, Sugita S, Nakamura T, Hiroi T, Morota T, Popescu M, Michikami T, Kitazato K, Matsuoka M, Kameda S, Honda R, Yamada M, Sakatani N, Kouyama T, Yokota Y, Honda C, Suzuki H, Cho Y, Ogawa K, Hayakawa M, Sawada H, Yoshioka K, Pilorget C, Ishida M, Domingue D, Hirata N, Sasaki S, de León J, Barucci MA, Michel P, Suemitsu M, Saiki T, Tanaka S, Terui F, Nakazawa S, Kikuchi S, Yamaguchi T, Ogawa N, Ono G, Mimasu Y, Yoshikawa K, Takahashi T, Takei Y, Fujii A, Yamamoto Y, Okada T, Hirose C, Hosoda S, Mori O, Shimada T, Soldini S, Tsukizaki R, Mizuno T, Iwata T, Yano H, Ozaki M, Abe M, Ohtake M, Namiki N, Tachibana S, Arakawa M, Ikeda H, Ishiguro M, Wada K, Yabuta H, Takeuchi H, Shimaki Y, Shirai K, Hirata N, Iijima Y, Tsuda Y, Watanabe S, Yoshikawa M (2021) Collisional history of Ryugu's parent body from bright surface boulders. *Nature Astron* 5:39–45. <https://doi.org/10.1038/s41550-020-1179-z>
- Tatsumi E, Domingue D, Hirata N, Kitazato K, Vilas F, Lederer S, Weissman PR, Lowry SC, Sugita S (2018) Vis-NIR disk-integrated photometry of asteroid 25143 Itokawa around opposition by AMICA/Hayabusa. *Icarus* 311:175–196. <https://doi.org/10.1016/j.icarus.2018.04.001>
- Tatsumi E, Popescu M, Campins H, de León J, García JL, Licandro J, Simon AA, Kaplan HH, DellaGiustina DN, Golish DR, Lauretta DS (2021) Widely distributed exogenic materials of varying compositions and morphologies on asteroid (101955) Bennu. *Monthly Not Royal Astron Soc* 508(2):2053–70
- Théret N, Cucchetti E, Robert E, Virmondois C, Millancourt C, Douaglin Q, Amsili A, Belloir J-M, Amilineni S, Khoory M et al (2024) Enhanced image processing for the caspex cameras onboard the rashid-1 rover. *Space Sci Rev* 220(5):60
- Ulamet S, Michel P, Grott M, Böttger U, Schröder S, Hübers H-W, Cho Y, Rull F, Murdoch N, Vernazza P, Prieto-Ballesteros O, Biele J, Tardivel S, Arrat D, Hagelschuer T, Knollenberg J, Vivet D, Sunday C, Jorda L, Groussin O, Robin C, Miyamoto H (2023) Science objectives of the MMX rover. *Acta Astronaut* 210:95–101. <https://doi.org/10.1016/j.actaastro.2023.05.012>
- Vernazza P, Binzel RP, Rossi A, Fulchignoni M, Birlan M (2009) Solar wind as the origin of rapid reddening of asteroid surfaces. *Nature* 458(7241):993–995. <https://doi.org/10.1038/nature07956>
- Vernazza P, Fulvio D, Brunetto R, Emery JP, Dukes CA, Cipriani F, Witasse O, Schaible MJ, Zanda B, Strazzulla G, Baragiola RA (2013) Paucity of tagish lake-like parent bodies in the asteroid belt and among jupiter trojans. *Icarus* 225(1):517–525. <https://doi.org/10.1016/j.icarus.2013.04.019>
- Vernazza P, Castillo-Rogez J, Beck P, Emery J, Brunetto R, Delbo M, Marsset M, Marchis F, Groussin O, Zanda B, Lamy P, Jorda L, Mousis O, Delsanti A, Djouadi Z, Dionnet Z, Borondics F, Carry B (2017) Different origins or different evolutions? decoding the spectral diversity among c-type asteroids. *Astron J* 153(2):72. <https://doi.org/10.3847/1538-3881/153/2/72>
- Virmondois C (2024) CASPEX: Camera for space exploration. *Space Sci Rev*
- Wang X, Schwan J, Hsu HW, Grün E, Horányi M (2016) Dust charging and transport on airless planetary bodies. *Geophys Res Lett* 43(12):6103. <https://doi.org/10.1002/2016GL069491>
- Xu J, Wang M, Lin H, Xu X, Liu B, Yan W, Yang Y, Wang R, Liu C, Xu R, He Z (2022) In-situ photometric properties of lunar regolith revealed by lunar mineralogical spectrometer on board Chang'e-5 lander. *Geophys Res Lett* 49(4):e2021GL096876
- Xu T, Cai W, Shu M, Zhang X, Zhang P, Liu C, Yang H, Wu Y (2023) Disk-integrated and disk-resolved photometry of the Moon with GaoFen-4 space observations. *icarus* 405:115696. <https://doi.org/10.1016/j.icarus.2023.115696>

Publisher's Note

Springer Nature remains neutral with regard to jurisdictional claims in published maps and institutional affiliations.